Journal of Sound and Vibration (1997) **203**(5), 867–888

EXPERIMENTAL ANALYSIS OF WAVE PROPAGATION IN RAILWAY TRACKS

D. J. THOMPSON†

TNO Institute of Applied Physics (*TPD*), *P.O. Box* 155, 2600 *AD Delft*, *The Netherlands*

(*Received* 28 *August* 1996, *and in final form* 3 *January* 1997)

Measurements of the vibrational behaviour of railway track are presented. Because the track system is effectively infinite, its motion consists of propagating waves, and usual modal analysis concepts and techniques are not appropriate. New experimental techniques are therefore developed to handle these phenomena. In particular the various propagating vibrational waves in the rail are identified in terms of their complex propagation coefficients and their corresponding deformed shapes. These waves are separated by using an analysis based on fitting a series of complex exponential functions to the measured data. Some predictions of wave phenomena in track are also presented for comparison and good agreement between theory and experiment is found.

1. INTRODUCTION

The dynamic behaviour of railway track in the frequency region 100–5000 Hz is of great importance in relation to the generation of noise by moving trains [1, 2]. The high frequency dynamics of the track at the excitation point play an important role in the wheel-rail interaction [3]. As well as this, the track itself is a significant source of the radiated noise [4–6]. Typically, in the frequency range between about 500 and 1600 Hz, the vibrations of the rail are the dominant source of noise. At higher frequencies, the wheel radiation becomes dominant, although the rail radiation remains important. The sleeper is the dominant source at lower frequencies, the exact frequency range being determined by the rail fastener stiffness [6].

Various theoretical models for the dynamic behaviour of track have been developed (see e.g., reference [7]). The level of detail required depends on the frequency range of interest. In the vertical direction, the track system can be modelled reasonably well at low frequencies by a beam on a continuous spring-mass-spring support, representing rail-pad, sleeper and ballast respectively [8]. The Timoshenko beam formulation (including shear deformation and rotational inertia) is required for frequencies above around 500 Hz. The discrete nature of the support system only has a significant effect at or around frequencies where the distance between sleepers corresponds to half a wavelength in the rail, or to multiple half-wavelengths (called "pinned-pinned" frequencies), the first of which occurs for the vertical direction between about 800 and 1200 Hz. Models including these effects can be found in references [8, 9].

Figure 1 illustrates how the simple beam formulation breaks down at higher frequencies. These results are examples of predictions made by using the finite element method, in which the modes of vibration of a particular length of rail are calculated with symmetry

† Current address: Institute of Sound and Vibration Research, University of Southampton, Highfield, Southampton SO17 1BJ, England.

0022–460X/97/250867 + 22 $25.00/0/sv970903

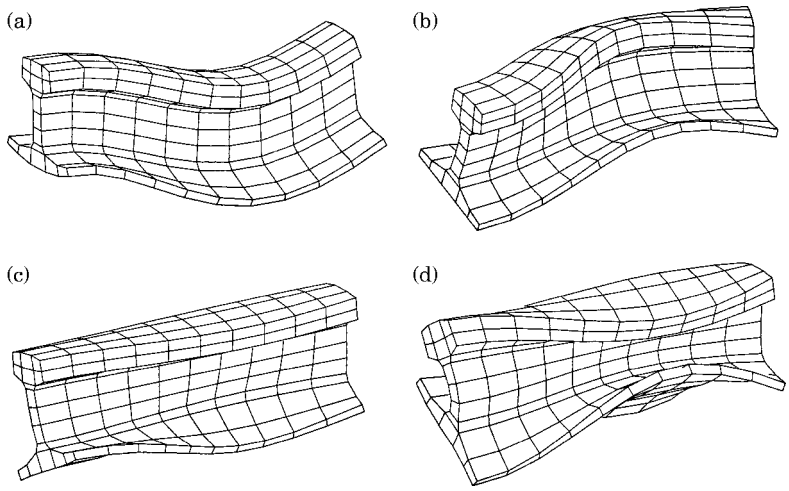

Figure 1. Waves in a free UIC54 rail predicted using a finite element model. In each case the mesh length is 0·54 m and the wavelength is 0·72 m. (a) 2149 Hz; (b) 1170 Hz; (c) 1705 Hz; (d) 2659 Hz.

and/or anti-symmetry boundary conditions at the ends. These modes (which are standing waves) are directly equivalent to travelling waves in an infinite rail with the same wavelength, which will occur at the frequency shown (the natural frequency of the finite length of rail).

Although useful for predicting free wave phenomena, this finite element model cannot be used to predict frequency responses, however, as the boundary conditions imply an infinite array of forces. Much more complex finite element models are possible in which the sleepers are also included and many bays are modelled; see, e.g., reference [10]. In references [1, 2] an alternative model was developed in which periodic structure theory is used. In this the rail was seen as a "periodic" structure with (arbitrary) period 10 mm, this length of rail being modelled by finite elements. The railpad-sleeper-ballast system was also introduced, although only as an equivalent continuous support. Other models have also been developed for a rail using for example a finite element method with harmonic continuation for the longitudinal direction [11, 12] (although the models in references [11, 12] are of the rail and did not include the support).

In these various models, railway track is seen as effectively infinite in nature and therefore its motion is not made up of normal modes of vibration but of a series of travelling waves. Note that models which truncate the track at a particular length artificially introduce modal behaviour, but if the model is long enough it can approximate travelling wave phenomena. These waves can occur at all frequencies above their particular "cut-on" frequency, which is effectively a resonance of the two-dimensional cross-section of the system, the motion of which may be both in-plane and in the direction perpendicular to the cross-section. Various near-field "waves" also occur, with amplitudes decaying rapidly away from the excitation point.

Despite the development of various models for wave phenomena in rails, experimental validation of these wave phenomena is so far limited to laboratory measurements on an unsupported length of rail (see, e.g., reference [13]). The purpose of the work presented in this paper is to quantify the wave behaviour by using measured data taken on track. In order to analyze these wave phenomena, standard modal analysis techniques are inadequate, since discrete normal modes are assumed rather than propagating waves which can occur at any frequency. New analysis techniques have therefore been developed, by

using which it is possible to verify the wave phenomena predicted by the theoretical models.

2. MEASUREMENTS

2.1. DESCRIPTION OF THE MEASUREMENTS

Detailed *in situ* measurements of the vibrational behaviour of three different types of railway track were carried out in October 1992 (see also references [5, 14]). Measurements were carried out prior to that on various other tracks, and the results from one of them, measured in April/May 1991 are also included here. These tracks were all of normal ballasted construction, with a nominal sleeper spacing of 0·6 m. Their properties are summarized in Table 1. The pad and ballast stiffnesses are derived from fitting theoretical curves to measured frequency responses and adjusting these parameters until a reasonable agreement is achieved (see also reference [7]). The ballast stiffness in particular is complex with a high loss factor—the values quoted here are the magnitudes, and differ from the real parts quoted in reference [14].

The selection includes three sleeper types, and three rail types: the UIC54E profile differs from UIC54 in having a narrower foot (125 mm compared to 140 mm) and head but is 2 mm taller. All rails were not new but the degree of wear was not recorded. The rail-pads of track C appear to be reasonably soft in the vertical direction while tracks A and E have rather stiff rail-pads (E is rather soft laterally however). In the case of track B (wooden sleeper), the fastening system does not include any elastomeric rail-pads although the local stiffness of the sleeper provides some resilience.

A mesh of nine accelerometers was placed on the rail between two sleepers, of which five have been used during lateral excitation and six during vertical excitation (see Figure 2). For each of positions 3 and 5 the analogue signals from two accelerometers were added electronically (and divided by 2) before recording to remove the rotational part of the signal. Thus only four signals were recorded for vertical excitation. For practical reasons an instrumented hammer was used for the excitation, the measurements being made between the passage of trains on an unloaded track. Valid measurements were possible up to 5–6 kHz, depending on the hammer tip used. For each measurement the results from 10 impacts were averaged. The various signals were tape recorded and then

TABLE 1

Summary of properties of the tracks measured

Parameter	Track			
	A	B	C	E
Rail type	UIC54E	UIC54E	UIC60	UIC54
Rail mass (kg/m)	54	54	60	54
Fastener	Nabla	K	Vossloh	DE clips
Pads	4·5 mm grooved	none	6 mm resilient	4·5 mm cork-rubber
Pad stiffness, vertical (N/m)	$1{\cdot}3 \times 10^9$	5×10^8	$3{\cdot}5 \times 10^8$	$9{\cdot}0 \times 10^8$
Pad stiffness, lateral (N/m)	$1{\cdot}0 \times 10^8$	$1{\cdot}77 \times 10^8$	$5{\cdot}0 \times 10^7$	$5{\cdot}0 \times 10^7$
Sleeper type	bibloc concrete	wood	monobloc concrete	bibloc concrete
Sleeper mass, 1/2 sleeper (kg)	122	30	162	120
Ballast stiffness magnitude vertical (N/m)	$1{\cdot}5 \times 10^8$	1×10^8	7×10^7	–
Ballast stiffness magnitude lateral (N/m)	$7{\cdot}5 \times 10^7$	1×10^8	$1{\cdot}1 \times 10^8$	–

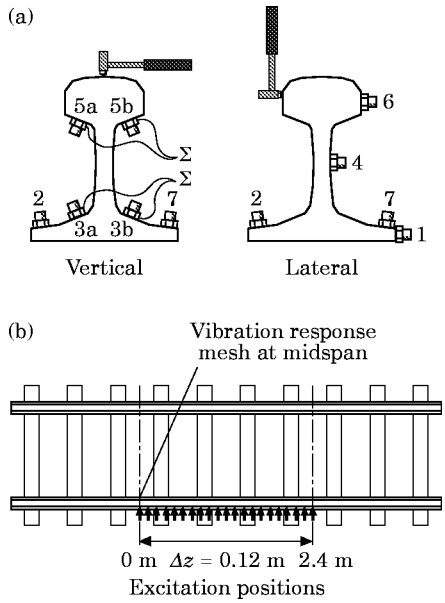

Figure 2. Measurement positions; (a) force and response positions on a cross-section for vertical and lateral excitation; (b) measurement sections along the rail.

analyzed in the laboratory by using a multi-channel digital Fourier analyzer. The rail was excited on the railhead in the vertical and lateral directions at positions spaced 12 cm apart up to a position 2·4 m from the response cross-section (see Figure 2). This was considerably easier to carry out than keeping the force position fixed and moving the response cross-section, but by reciprocity gives virtually equivalent results.

2.2. FREQUENCY RESPONSE FUNCTIONS

Figures 3 and 4 show examples of the measured vertical and lateral frequency responses for track E at the midspan position. These are point accelerances—acceleration divided by force as a function of frequency. A lack of resonant behaviour can be seen which is characteristic of an infinite waveguide. A distinct peak can be seen at around 1 kHz in the vertical response and to a lesser extent in the lateral response around 500 and 700 Hz. These are ''pinned-pinned'' frequencies.

For comparison, examples are also shown of point accelerances predicted by using a continuously supported track model from references [1, 2]. This model includes cross-sectional deformation of the rail. The sharp peak seen 1 kHz in the measurements (the ''pinned-pinned'' effect) is not found in the predictions, and the level is underpredicted between 500 and 1500 Hz. However, a model which includes the periodic support of the rail [15] gives an extremely good prediction of the vertical accelerance.

For the lateral direction the agreement between measurement and prediction is reasononable. In fact there was little difference between measurements above a sleeper and at mid-span. The remaining difference in level between measurement and prediction is caused by the different locations of excitation/response point—this is located at the centre of the head in the measurements and at the top in the predictions.

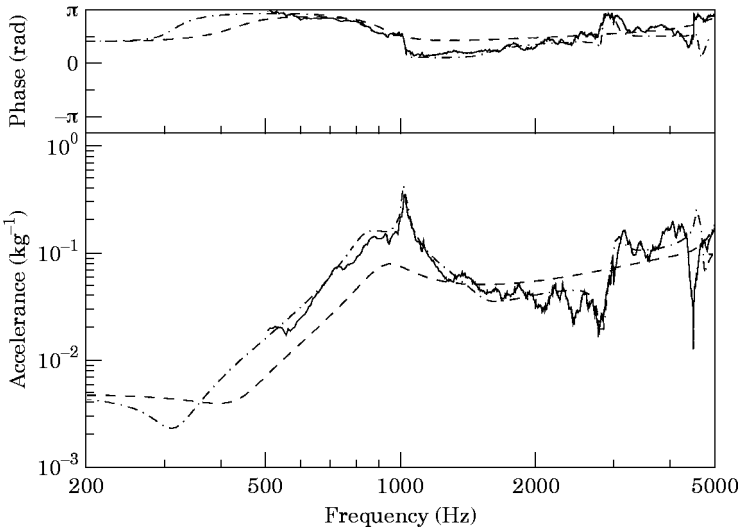

Figure 3. Vertical point accelerances for track E, measured, and predicted by using various theoretical models. ——, measured between sleepers; – – –, continuously supported rail with cross-section deformation; –·–·–, discretely supported Timoshenko beam (between sleepers).

Equivalent results for tracks A–C have already been published in references [14, 15] including comparisons between measurements and predictions.

3. WAVE ANALYSIS

3.1. METHOD

A method will now be derived which allows the response in each of the various propagating waves in the track to be separated from the frequency response functions described above (measured for response at the midspan position and for the various excitation positions).

Initially it was considered that the wavenumbers could be separated from the

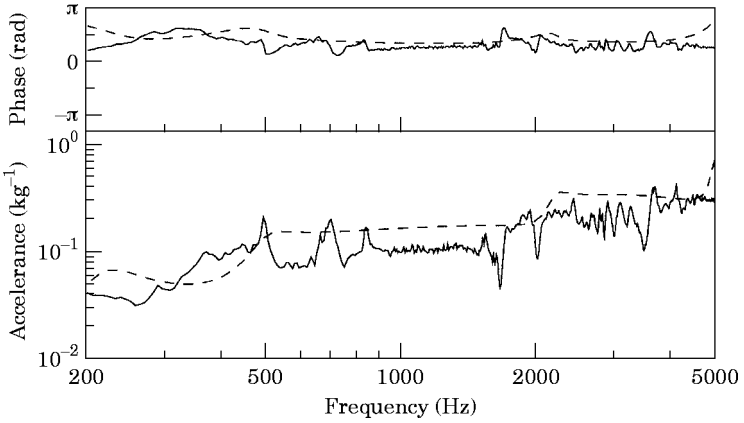

Figure 4. Lateral point accelerances for track E, measured, and predicted by using a theoretical model. ——, measured between sleepers; – – –, continuously supported rail with cross-section deformation.

measured data by using a spatial Fourier transform. However this has the serious limitation that, for the selected measurement grid with 21 excitation positions spaced 0·12 m apart, the wavenumber resolution is very limited, with only 11 discrete values (0, 2.62, . . . , 26.2 rad/m, since $2\pi/2{\cdot}4 = 2{\cdot}62$) along with their negative counterparts. The use of Fourier transforms also implicitly assumes periodicity beyond the measurement section, which is not valid for the decaying travelling waves which are expected.

An alternative method has therefore been developed, which makes explicit use of the form of the motion. This method has been derived from the time-domain curve-fitting procedure which is used in modal analysis [16]. At each frequency, the response $h_j(z)$ at position j ($j = 1, \ldots, J$; $J \leqslant 7$) on the cross-section and distance z from the applied force can be written as an infinite sum of exponential functions:

$$h_j(z) = \sum_{n=1}^{\infty} A_{nj}\, \mathrm{e}^{s_n z} \tag{1}$$

where $s_n = -\beta_n - \mathrm{i}k_n$ is the complex propagation coefficient (k_n is the wavenumber and β_n represents the decay with distance). The decay with distance of wave n (in dB/m) given by

$$D_n = -20 \log_{10} |\mathrm{e}^{s_n}| = 8{\cdot}686\beta_n. \tag{2}$$

A_{nj} is the associated (complex) amplitude at position j on the cross-section. This represents the deformed shape of the cross-section, and when normalized is equivalent to a modeshape, except that it exists for, and is different for every frequency.

Equation (1) strictly applies only to a continuously supported rail; for a periodically supported rail, the amplitude A_{nj} is a periodic function of z with period L, the distance between supports. Even if strong periodicity occurs in these amplitudes, however, the method described here will give an average amplitude A_{nj} over the period L, and should still give reliable estimates for the propagation coefficients s_n. The possible effects of periodicity are discussed later.

The complete set of transfer functions, measured at positions $z_q = (q-1)\Delta z$ (for $q = 1, \ldots, Q$) can be approximated by limiting equation (1) to a finite sum over N waves:

$$h_{qj} = h_j(z_q) \approx \sum_{n=1}^{N} A_{nj}\, \mathrm{e}^{s_n (q-1)\Delta z}. \tag{3}$$

Here h_{qj} are known functions, whilst A_{nj} and s_n are unknowns. Equation (3) is solved for A_{nj} and s_n by using a procedure based on the Prony method, as used in reference [16] for fitting sums of decaying exponential functions to impulse response functions in the time domain. This procedure, which is described in the Appendix, has been modified for the current application to derive a least-squares solution to an overdetermined set of equations. It is important to note here that the Q measurement positions must be equally spaced to use this method.

For a given response position j, equation (3) represents Q equations with $2N$ complex unknowns (A_{nj} and s_n), so this imposes a limit on N of $2N \leqslant Q$. The maximum number of waves which can be fitted to the data available from $Q = 21$ positions for

a single j is therefore 10. However, unlike the spatial Fourier transform approach referred to earlier, the wavenumbers k_n can take any value between $\pm\pi/\Delta z$. A Fourier transform approach would also not have produced the decaying part of the propagation coefficients, β_n.

To improve the statistical reliability, the fit has been based on a reduced number of waves: $N = 7$ for lateral motion and $N = 5$ for vertical motion, these values being chosen a little larger than what is expected on the basis of theoretical predictions [1]. Furthermore the solution derived in the Appendix is found for all J chosen positions on the cross-section, j, simultaneously, which also increases the statistical degrees of freedom.

Since the analysis is based on a predefined number of waves N at each frequency, some of the waves extracted by the analysis, particularly those with large β_n may be "fictitious" waves, by analogy with fictitious modes in modal analysis [16]. In order to be able to recognize the significant results, the relative importance of the various waves (at each frequency) is found by deriving the proportion of vibration "energy" per wave:

$$P_n = E_n \Big/ \sum_{n'=1}^{N} E'_n \quad \text{where } E_n = \sum_{j=1}^{J} \sum_{q=1}^{Q} |A_{nj}|^2 \, \mathrm{e}^{-2\beta_n(q-1)\Delta z}. \tag{4}$$

E_n is proportional to the sum of the "energy" in wave n in each of the 21 measurement cross-sections. Waves with a high attenuation rate will have a lower value of E_n as will those with low amplitudes, A_{nj}. Those waves with larger values of P_n can be considered to be more reliable than those with a small proportion of the energy.

3.2. RESULTS

Of the transfer accelerances obtained between 0 and 2·4 m, five response positions on the cross-section have been used for lateral excitation (1, 2, 4, 6 and 7) and four positions

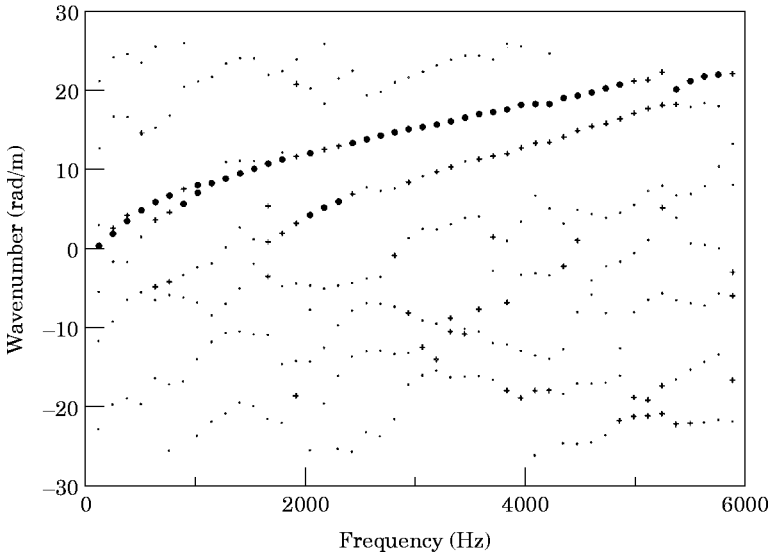

Figure 5. Measured imaginary parts of propagation coefficients (wavenumbers) for track B for lateral excitation; ● >40%, + 10–40% and · <10% of vibrational energy.

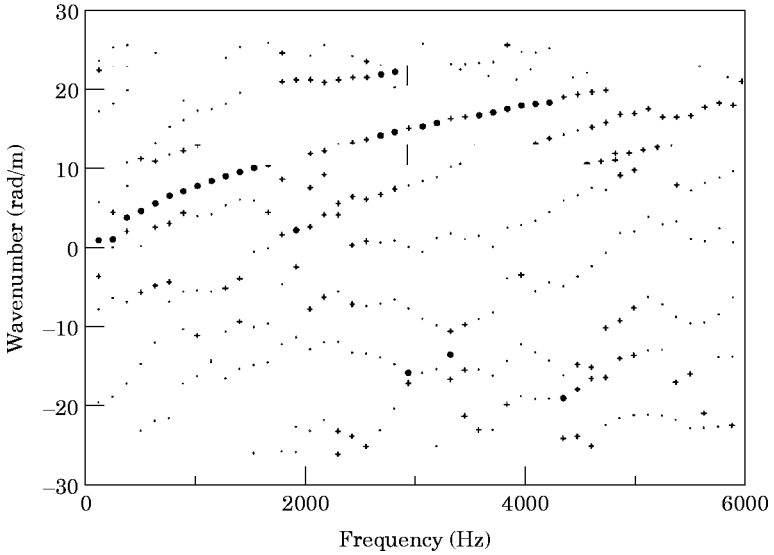

Figure 6. Measured imaginary parts of propagation coefficients (wavenumbers) for track A for lateral excitation. Key as in Figure 5.

have been used for vertical excitation (2, 3, 5 and 7). Due to technical problems, the data for points 3 and 5 at track E were not correctly measured and therefore had to be omitted. To simplify the analysis and reduce the number of results, groups of 16 adjacent frequency lines have been combined, giving an effective bandwidth of 100 Hz for track E where the original bandwidth was 6·25 Hz, and 128 Hz for tracks A–C where the original bandwidth was 8 Hz.

3.2.1. *Lateral excitation*

The wavenumbers (imaginary parts of the complex propagation coefficients) for lateral

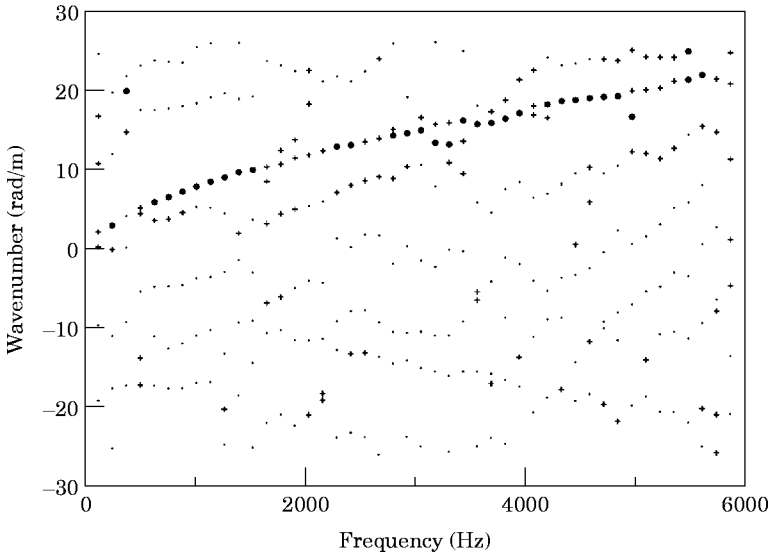

Figure 7. Measured imaginary parts of propagation coefficients (wavenumbers) for track C for lateral excitation. Key as in Figure 5.

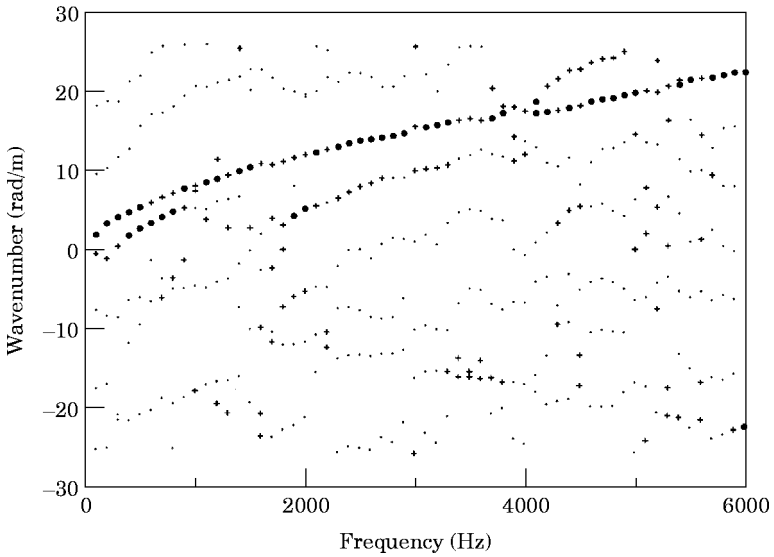

Figure 8. Measured imaginary parts of propagation coefficients (wavenumbers) for track E for lateral excitation. Key as in Figure 5.

excitation are presented in Figures 5–8. The 12 cm spacing chosen limits the wavenumber range to $\pm 26{\cdot}2$ rad/m, beyond which the data are subject to aliasing. The points are marked by using different symbols according to the proportion of vibration "energy" in a given wave, equation (4). Note that the analysis for each (100 or 128 Hz) frequency band is independent, so it is not possible to relate directly waves at one frequency with those at the next. This can mostly be done by eye, however, and comparison with theoretical results also aids interpretation.

Of the waves which are most clearly defined (consistently above 10% of the energy),

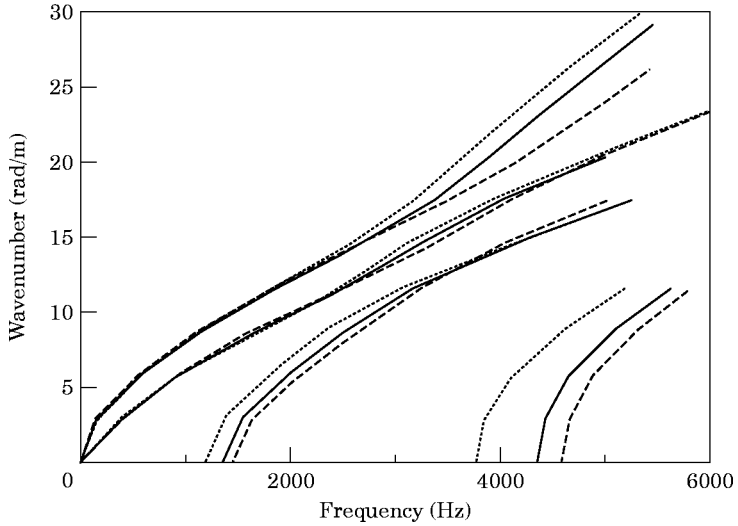

Figure 9. Wavenumbers for lateral waves predicted by finite element calculations of free rail; ——, UIC54 (track E); – – –, UIC54E (tracks A and B); ····, UIC60 (track C).

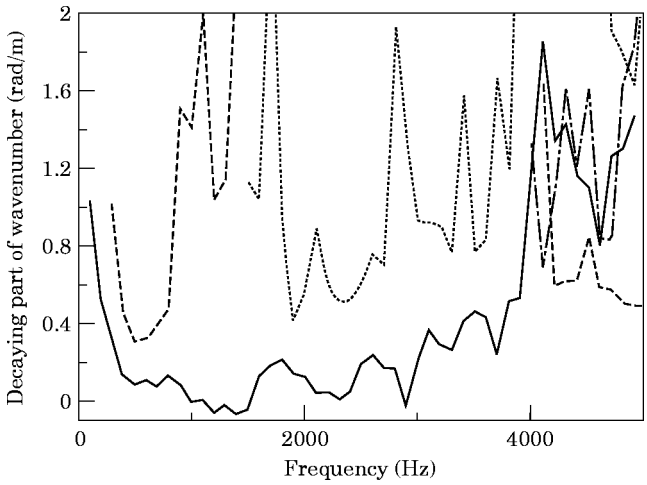

Figure 10. Measured decaying part of propagation coefficient (β_n) for track E for lateral excitation. ——, Wave 1; – – – – –, wave 2; ····, wave 3; — — — —, wave 4.

one wave can be seen to propagate from low frequencies, cutting on at around 200 Hz. A second wave cuts on around 400 Hz, although it is not seen so consistently—it is clearest for track E. For all tracks this second wave has a much lower amplitude above about 800 Hz and is not seen at all between 1·5 and 4 kHz (3 kHz for track C). A third wave begins at 1·7 kHz for the 54 kg/m rails and 1·4 kHz for UIC 60 rail. Higher order waves found in the predictions [2] are not found consistently in the measured data. In the region 5–6 kHz some aliasing is observed, in which waves with a wavenumber greater than $\pi/\Delta z = 26{\cdot}2$ rad/m appear as large negative wavenumbers. To obtain more reliable measurements above 5 kHz, a spacing closer than 12 cm should have been used.

Predicted results from finite element model of Figure 1 are given in Figure 9 for all three types of rail. The mesh length (0·54 m) limits the wavenumbers which can be calculated to multiples of $\pi/1{\cdot}08 = 2{\cdot}9$ rad/m. The lack of rail-pads, sleepers, etc., in this model means that the first two waves (lateral bending and torsion) cut-on at 0 Hz in the predictions,

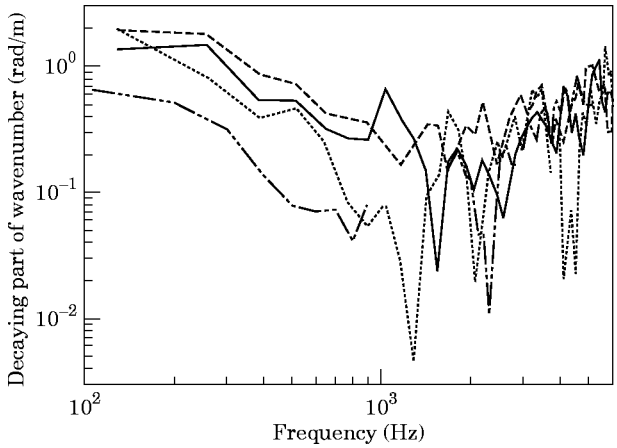

Figure 11. Minimum measured decaying part of propagation coefficient (β_n) for each track for lateral excitation. – – –, Track A; ——, track B; ····, track C; — — — —, track E.

and the third wave also cuts on at a slightly lower frequency than in the measurements. Nevertheless, the trends are the same as those found in Figures 5–8.

The real parts of the propagation coefficients are shown in Figure 10 for track E, in which the results for the various wave types have been connected up manually from an analysis of the wavenumbers shown of Figure 8. The first wave (the one with the highest wavenumber at a given frequency) has the lowest attenuation up to 4 kHz. Between 1 and 1·5 kHz the attenuation is negative which is not physically possible. It should be noted that a decay of less than about 0·5 dB/m is too low to measure accurately over 2·4 m—a longer measurement grid would be necessary. This corresponds to a value of β_n of about 0·06.

For only the waves with significant "energy" at each frequency, the minimum value of the decaying part of the wave propagation coefficient (β_n) has been determined for each track. This is shown in Figure 11. In all cases this corresponds to the lateral wave with the highest wavenumber k_n in the region 400–4000 Hz (3000 Hz for track C). The negative values for track E are omitted from this logarithmic presentation. For tracks A–C the attenuations are not negative, but some isolated low values occur which are below the limit of reasonable accuracy. At high frequencies the tracks all have similar decay rates, but at low frequencies tracks E and C, which have the lowest lateral pad stiffness (see Table 1), have lower attenuation of the lateral waves than tracks A and B.

The cross-sectional deformations of the various lateral waves can be derived from the relative amplitude and phase of A_{nj} at the five measurement positions. These are shown in Figure 12 for track E for selected frequencies. The first wave is seen to consist of lateral bending at low frequencies but changes to a foot-rocking motion at high frequencies. The second wave begins as a torsional wave, and the third as a bending of the web. Figure 13

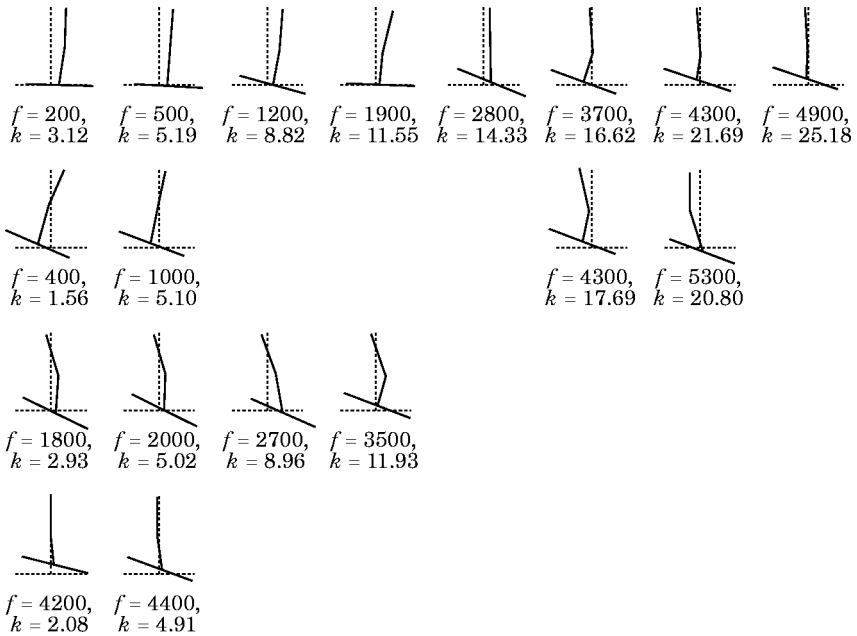

Figure 12. Normalized cross-section deformation associated with each lateral wave, at selected frequencies, f in Hz, from experimental analysis for track E. Wavenumbers, k, in rad/m are also listed.

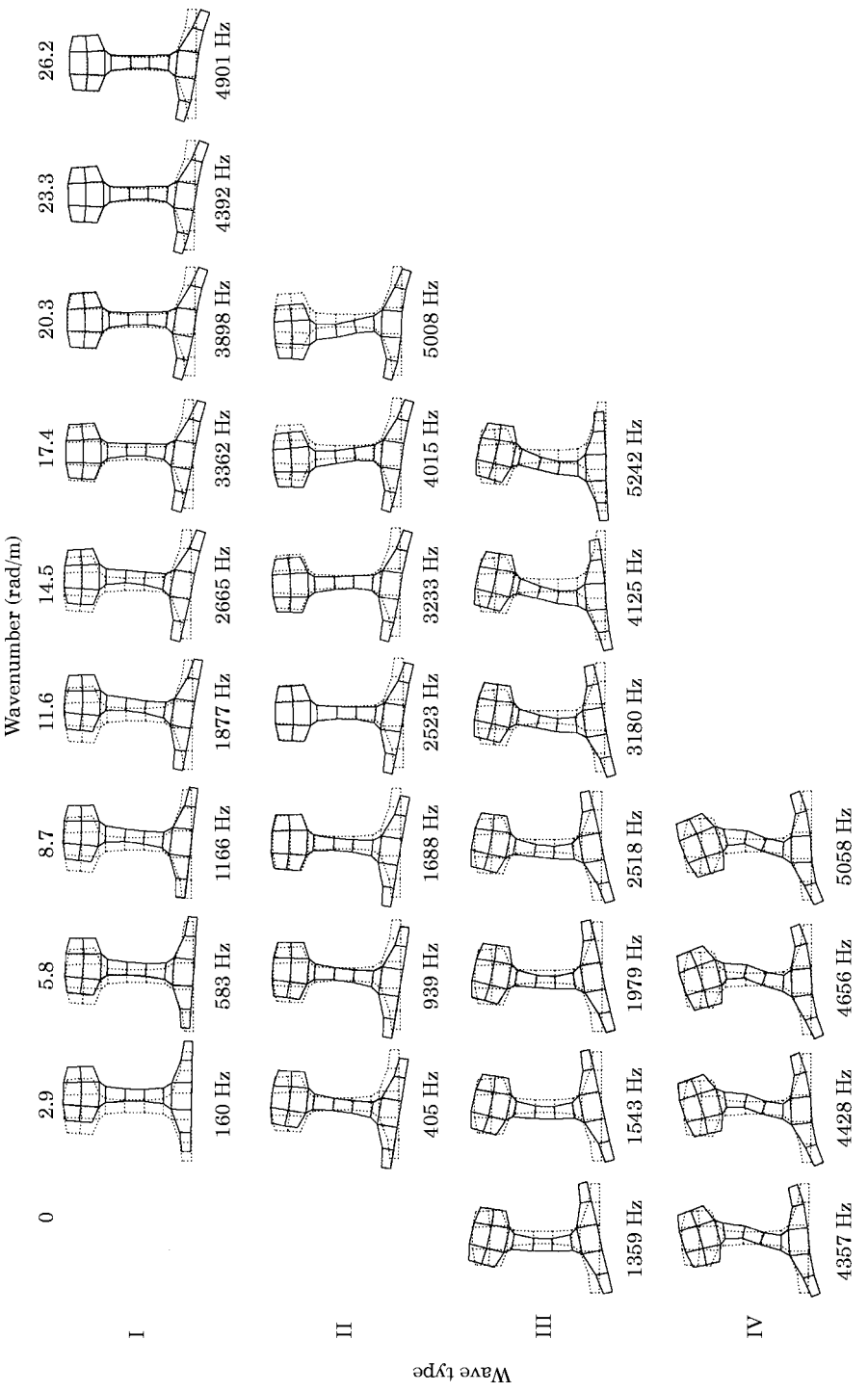

Figure 13. Normalized cross-section deformation associated with each lateral wave, at selected frequencies, from finite element prediction for track E (free rail).

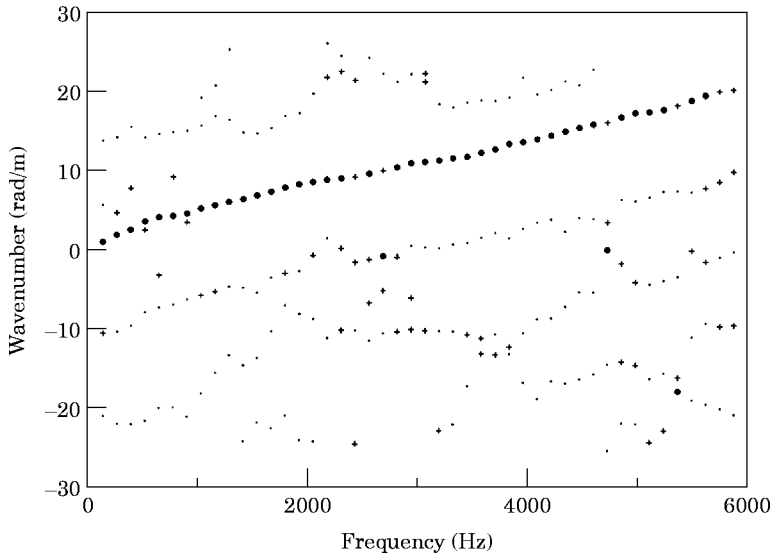

Figure 14. Measured imaginary parts of propagation coefficients (wavenumbers) for track B for vertical excitation. Key as in Figure 5.

gives equivalent results from a finite element calculation (equivalent to Figure 1), which are remarkably similar to those observed. From these predicted results it can be seen that the second wave has relatively small amplitudes on the rail head between about 1·5 and 4 kHz, which explains why it was not identified in the experiments in this frequency range (excitation was always on the middle of the head in the experiments). A fourth lateral wave is predicted above about 5 kHz but is not found in the measurements; this also has a node near the excitation point.

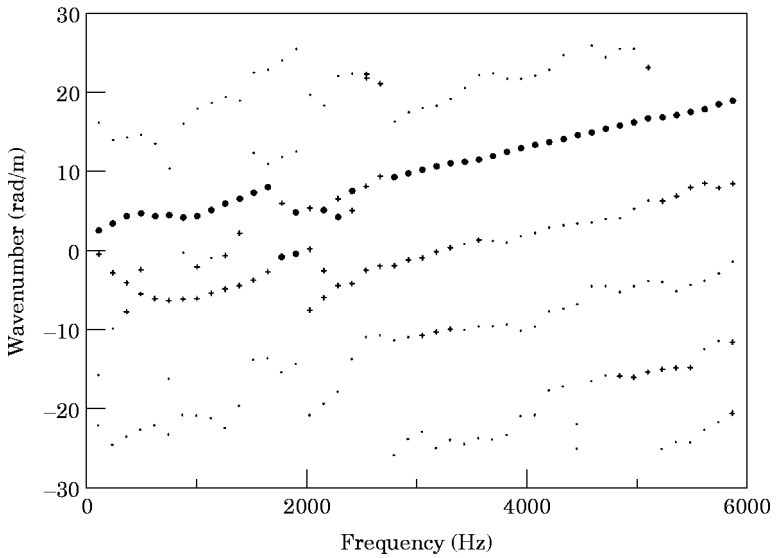

Figure 15. Measured imaginary parts of propagation coefficients (wavenumbers) for track A for vertical excitation. Key as in Figure 5.

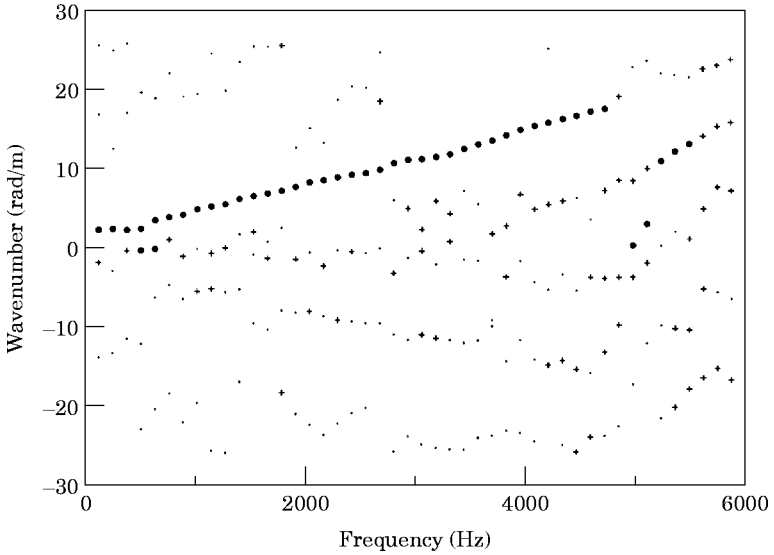

Figure 16. Measured imaginary parts of propagation coefficients (wavenumbers) for track C for vertical excitation. Key as in Figure 5.

3.2.2. *Vertical excitation*

Figures 14–17 show the wavenumber results for the vertical waves. Here a single wave dominates up to 4 kHz. Equivalent predicted results from the finite element model are given in Figure 18 for comparison. These include longitudinal waves, which have not been measured in the experimental arrangement described, as neither excitation nor response in the longitudinal direction have been included.

A higher order vertical wave cuts on around 5 kHz, and in fact is strongly coupled with

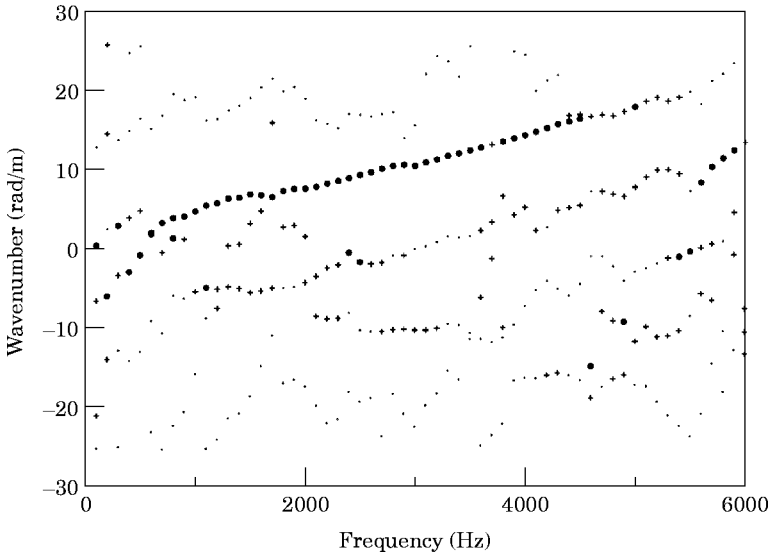

Figure 17. Measured imaginary parts of propagation coefficients (wavenumbers) for track E for vertical excitation. Key as in Figure 5.

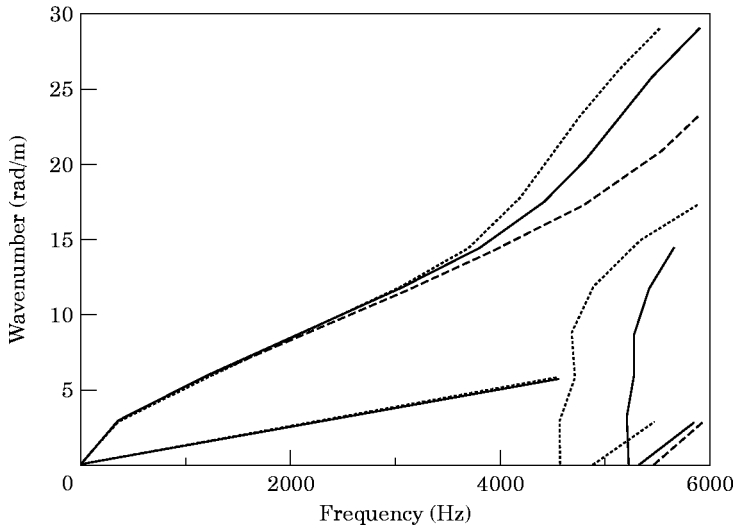

Figure 18. Wavenumbers for vertical and longitudinal waves predicted by finite element calculations of free rail; ——, UIC54 (track E); – – –, UIC54E (tracks A and B); ···, UIC60 (track C).

the longitudinal wave around 6 rad/m. This cannot be discerned in these results due to the limited wavenumber resolution of the finite element model, but it is clearly seen in the results in reference [2]. Consequently the two curves should not actually cross, but the wave cutting on at arount 5 kHz will follow the line of the longitudinal wave, while the longitudinal wave will follow the line of the former wave.

The predicted curves for the vertical bending wave show the same feature as the measured curve, namely that the UIC60 rail has the highest wavenumber at a given frequency, and the UIC54E rail the lowest. However, the measured wavenumbers are generally a little lower than those predicted for each rail.

The decaying part of the propagation coefficient of the dominant vertical wave, shown in Figure 19, is generally higher than for the dominant lateral waves, especially below

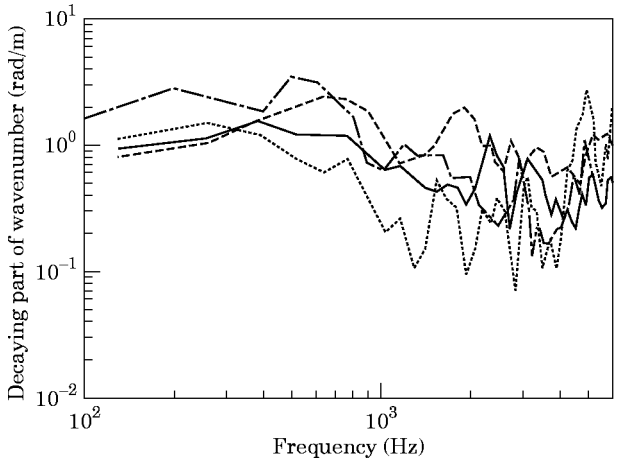

Figure 19. Minimum measured decaying part of propagation coefficient (β_n) for each track for vertical excitation: – – –, Track A; ——, track B; ····, track C; –·–·–, track E.

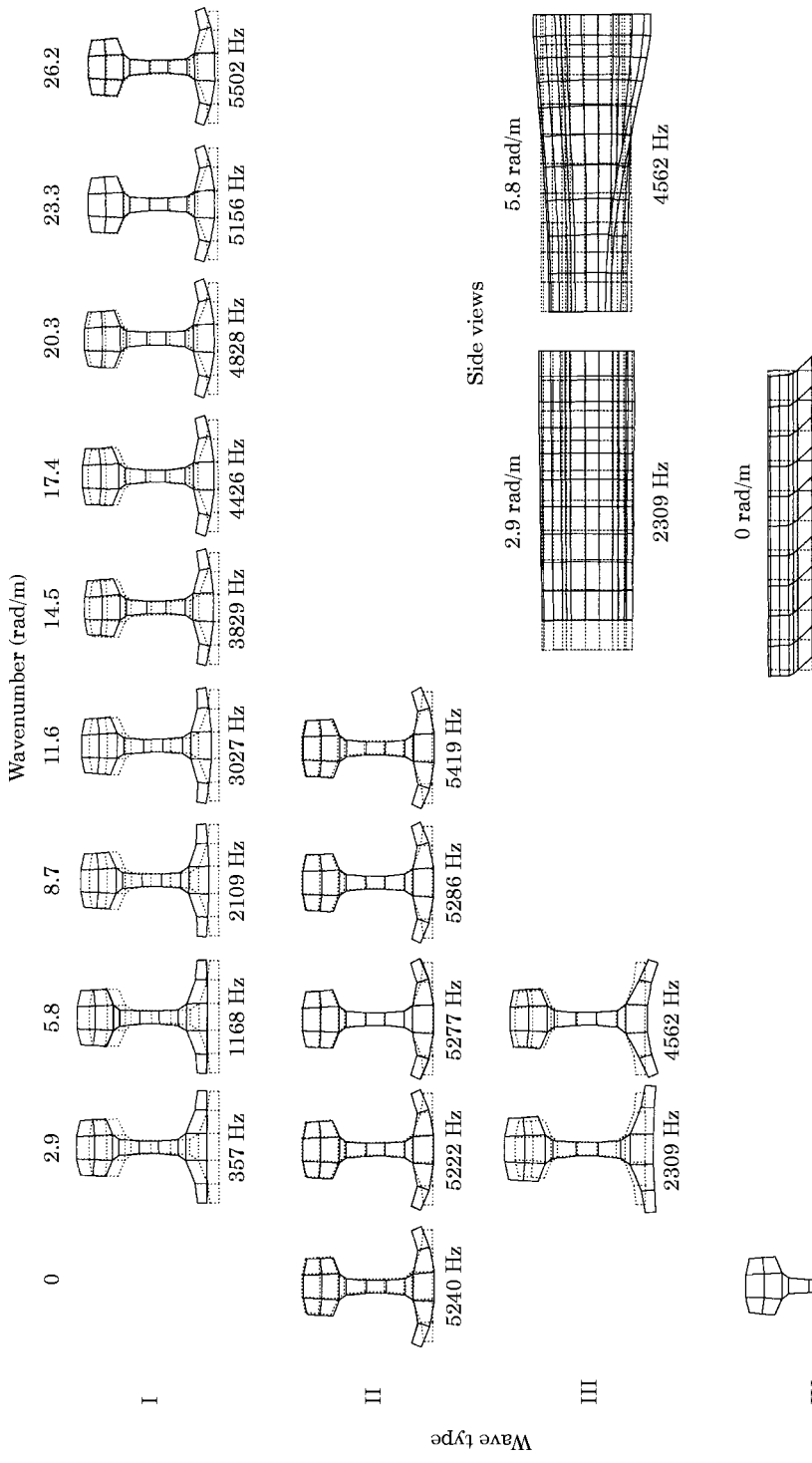

Figure 20. Normalized cross-section deformation associated with each vertical/longitudinal wave, at selected frequencies, from finite element prediction for track E (free rail).

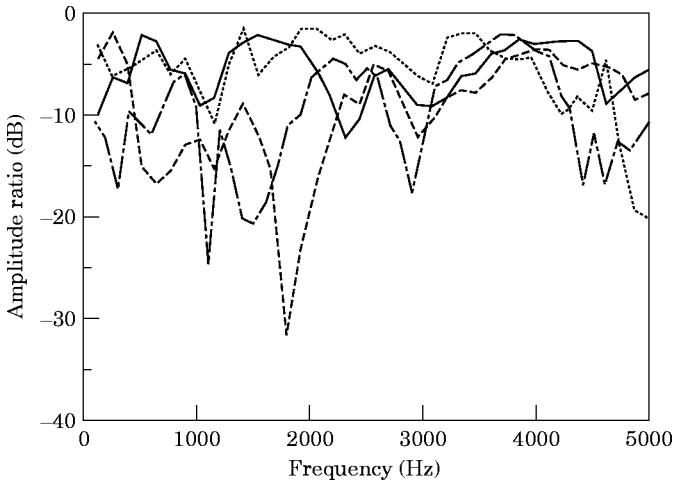

Figure 21. Logarithmic ratio of maximum to minimum amplitude within sleeper span measured for each track for vertical bending wave; – – –, Track A; ——, track B; ····, track C, –·–·–, track E.

1 kHz. Above 2 kHz, on the other hand, the vertical waves generally have a lower decay rate than the lateral waves. Track C has the lowest attenuation for the vertical direction. This is a consequence of the fact that it has the softest rail fasteners in this direction—see Table 1—as the damping in the track, at frequencies above the uncoupling frequency of the rail from the sleeper, is determined by the rail-pad stiffness and loss factor. Both of the bibloc sleepered tracks (A and E) contain a strong broad peak in the attenuation at around 500–700 Hz, corresponding to the sleeper and pad acting as a mass-spring dynamic absorber. After a dip around the pinned-pinned frequency (1 kHz), track A especially contains another peak around 1500 kHz. These features have also been found in predictions with a periodically supported beam model (see Figure 7 of reference [15]).

Figure 20 shows the cross-section deformations corresponding to the vertical and longitudinal waves predicted by the finite element calculation. An increasing amount of foot motion can be seen in each wave as frequency increases.

3.3. DISCUSSION

On further inspection, the measured vertical wavenumbers shown in Figures 14–17 can be seen to contain an interesting phenomenon. As well as the predominant vertical wave (k_1), a series of "shadow" waves are found, the dispersion curves of which run roughly parallel to that of k_1. These have the wavenumbers

$$k_n \approx k_1 + (2\pi/\Delta z)(n-1)/5, \tag{5}$$

for n an integer. The fact that these are spaced at one fifth of the total range of wavenumbers is indicative of a relation to the periodicity of the track support (since there are five excitation positions within each sleeper span). If the amplitude A_{nj} is not constant over a sleeper span, but periodic, these modulations of the amplitude will manifest themselves as additional wavenumber components as found in Figures 14–17. Nevertheless, the predominant wavenumber is almost always the one expected from the equivalent continuous track model.

Another phenomenon which might be expected to occur, is that a positive wavenumber k_1 may occur simultaneously with its negative counterpart $-k_1$ (due to reflections at the sleepers causing standing waves to occur). Whilst this does not occur to any large extent, it is nevertheless the case that the modulation effects noted above are often strongest when $-k_1$ is also one of the k_n's as given in equation (5), for example at 1 kHz (the first pinned-pinned frequency) where $k_1 = \pi/0{\cdot}6 = 5{\cdot}24$.

Such phenomena are not observed to the same degree in the lateral results (Figure 5–8), which is consistent with a much lesser effect of periodicity in this direction (a consequence of the lower support stiffnesses for this direction).

In order to quantify the modulation of the amplitude within a sleeper span in the vertical bending wave, a modified version of the analysis method has been applied in which, instead of $J = 4$ positions on $Q = 21$ cross-sections, the $Q = 4$ sleeper spans are used (i.e., with $\Delta z = 0{\cdot}6$) with $J = 4 \times 5$ positions within them. In this analysis, therefore, each position within the sleeper span is treated as independent. On the other hand, at most $N = 2$ waves can be extracted. One of these turned out always to correspond to the dominant vertical bending of wave of Figures 14–17. The corresponding deformed shape A_{nj} contains 4×5 positions.

Results are given here only in the form of the ratio between the smallest and largest amplitudes within a sleeper span. For each frequency, the mean is first determined of $|A_{nj}|$ over the four positions on each cross-section. The cross-section with the maximum such response is selected, as well as that with the minimum response. The ratio between these responses gives a measure of the modulation of the response within a sleeper span. This factor is shown in Figure 21 in decibels ($20 \log_{10} (A_{min}/A_{max})$). Two tracks (B and C) have rather low modulation whilst on the other two (A and E) it is somewhat higher. It is particularly high for track E (up to 30 dB) around the pinned-pinned frequencies, i.e., approximately 1 kHz and 2·9 kHz, and for track A around 1·8 kHz, the reason for which is less clear.

4. CONCLUSIONS

A new experimental analysis method has been developed for analyzing propagating waves in effectively infinite structures. Very little prior knowledge is required of the form of these waves, although the choice of mesh size can be optimized by knowledge of the likely range of wavenumbers.

Application of this method to railway track allows one vertical and three lateral propagating waves to be clearly identified, and their wavenumbers determined as a function of frequency up to 5 kHz. The deformed shapes and decay rates of each wave along the rail could also be measured. The cut-on frequencies of the vertical bending, lateral bending and torsional waves are in the range 200–500 Hz, depending on the fastener stiffness. The third lateral wave, which consists of bending of the web, cuts on at around 1·7 kHz for UIC 54 rail and 1·4 kHz for UIC 60 rail independently of fastener stiffness. The deformed shapes of each wave are frequency-dependent, making classification difficult; the measured shapes agree well with predictions, however. Higher order waves which are predicted to cut on at around 5 kHz in both lateral and vertical directions were not identified clearly in the measurements, probably due to the choice of excitation position.

The chosen mesh was only just sufficient for analysis of waves in the track up to 5 kHz, with some aliasing occurring above this frequency, indicating that a closer spacing would be desirable here. A longer mesh is required where the attenuation is lower than about

0·5 dB/m, which occurs for some of the lateral results. The number of measurement cross-sections determines the maximum number of waves which can be resolved, and this was more than enough. Additional excitation positions, for example on the web or foot, could be used to ensure that all waves are identified, but the results found are the most relevant for excitation due to wheel/rail contact.

ACKNOWLEDGMENTS

The measurements described here were carried out under contract for E.R.R.I. (the European Rail Research Institute) committee C163, in collaboration with Vibratec, Lyon, France. The assistance of the Dutch Railways (NS) in carrying out the measurements is gratefully acknowledged, as is the provision of tracks for measurements by German (DB), Swiss (SBB) and Dutch railways. From the TNO Institute of Applied Physics, W. J. A. van Vliet, M. G. Dittrich, F. J. W. Biegstraaten and M. H. A. Janssens who carried out much of the measurement work.

REFERENCES

1. D. J. Thompson 1990 *Ph.D. Thesis*, *University of Southampton*. Wheel-rail noise: theoretical modelling of the generation of vibrations.
2. D. J. Thompson 1993 *Journal of Sound and Vibration* **161**, 421–446. Wheel-rail noise generation, part III: rail vibration.
3. D. J. Thompson 1993 *Journal of Sound and Vibration* **161**, 387–400. Wheel-rail noise generation, part I: introduction and interaction model.
4. D. J. Thompson 1988 *Journal of Sound and Vibration* **120**, 275–280. Predictions of the acoustic radiation from vibrating wheels and rails.
5. D. J. Thompson, P. Fodiman and H. Mahé 1996 *Journal of Sound and Vibration* **193**, 137–147. Experimental validation of the TWINS prediction program for rolling noise, part 2: results.
6. N. Vincent, P. Bouvet, D. J. Thompson and P. E. Gautier 1996 *Journal of Sound and Vibration* **193**, 161–171. Theoretical optimization of track components to reduce rolling noise.
7. K. Knothe and S. L. Grassie 1993 *Vehicle System Dynamics* **22**, 209–262. Modelling of railway track and vehicle/track interaction at high frequencies.
8. S. L. Grassie, R. W. Gregory, D. Harrison and K. L. Johnson 1982 *Journal of Mechanical Engineering Science* **24**, 77–90. The dynamic response of railway track to high frequency vertical excitation.
9. M. A. Heckl 1992 *Proceedings of DAGA* 92, 1033–1036. Anregung von gekoppelten Wellen auf einem Timoshenko-Balken mit äquidistanten Stützstellen.
10. B. Ripke 1995 *VDI Fortschritt-Berichte*, *Reihe* 12 *Nr*. 249. Hochfrequente Gleismodelling und Simulation der Fahrzeug-Gleis-Dynamik unter Verwendung einer nichtlinearen Kontaktmechanik.
11. K. Knothe, Z. Strzyzakowski, K. Willner 1994 *Journal of Sound and Vibration* **169**, 111–123. Rail vibrations in the high frequency range.
12. L. Gavric 1995 *Journal of Sound and Vibration* **185**, 531–543. Computation of propagative waves in free rail using a finite element technique.
13. W. Scholl 1982 *Acustica* **52**, 10–15. Schwingungsuntersuchungen an Eisenbahnschienen.
14. N. Vincent and D. J. Thompson 1995 *Interaction of Railway Vehicles with the Track and its Substructure*, *Supplement to Vehicle System Dynamics* **24**, 100–114. Track dynamic behaviour at high frequencies. Part 2: experimental results and comparisons with theory.
15. D. J. Thompson and N. Vincent 1995 *Interaction of Railway Vehicles with the Track and its Substructure*, *Supplement to Vehicle System Dynamics* **24**, 86–99. Track dynamic behaviour at high frequencies. Part 1: theoretical models and laboratory measurements.
16. D. J. Ewins 1984 *Modal testing: theory and practice*. Letchworth, U.K.: Research Studies Press. See p. 180ff.

APPENDIX: LEAST-SQUARES SOLUTION FOR PROPAGATION COEFFICIENTS AND AMPLITUDES

The measurements yield a set of transfer accelerances, h_{qj}, measured for force positions $z_q = (q-1)\Delta z$ (for $q = 1, \ldots, Q$) relative to the response positions (j is the index over multiple response positions on a single cross-section). These accelerances can be approximated by a finite sum over N waves,

$$h_{qj} = h_j(z_q) \approx \sum_{n=1}^{N} A_{nj}\, \mathrm{e}^{s_n(q-1)\Delta z}, \tag{A1}$$

where $s_n = -\beta_n - \mathrm{i}k_n$ is the complex propagation coefficient (k_n is the wavenumber) and A_{nj} is the associated amplitude. Upon writing

$$v_n = \mathrm{e}^{s_n \Delta x} \tag{A2}$$

it follows that

$$h_{qj} \approx \sum_{n=1}^{N} A_{nj} v_n^{(q-1)}. \tag{A3}$$

Multiplying each equation by an unknown factor B_q and summing over q gives

$$\sum_{q=1}^{Q} B_q h_{aj} \approx \sum_{n=1}^{N} A_{nj} \sum_{q=1}^{Q} B_q v_n^{(q-1)}. \tag{A4}$$

A set of B_q is sought for which

$$\sum_{q=1}^{Q} B_q h_{qj} = 0 \tag{A5}$$

for all j. The set B_q is selected such that $B_q = 0$ for $q \geqslant N+2$ and $B_{N+1} = 1$. This gives

$$\sum_{q=1}^{N} b_q h_{qj} = -h_{(N+1)j} \tag{A6}$$

for all j. Since in general $A_n \neq 0$, it follows from equation (A4) that

$$\sum_{q=1}^{N+1} B_q v_n^{(q-1)} = 0 \tag{A7}$$

for each n. Similarly, for $r \geqslant 0$,

$$\sum_{q=1}^{N+1} B_q h_{(q+r)j} = \sum_{n=1}^{N} A_{nj} \left(\sum_{q=1}^{N+1} B_q v_n^{(q-1)} \right) v_n^r. \tag{A8}$$

The bracketed term is equal to zero from equation (A7), and hence

$$\sum_{q=1}^{N} B_q h_{(q+r)j} = -h_{(N+1)j} \quad 0 \leqslant r \leqslant Q - N - 1. \tag{A9}$$

Equation (A9) can be rewritten in matrix form as

$$\begin{bmatrix} h_{11} & \cdots & h_{N1} \\ \vdots & & \vdots \\ h_{(Q-N)1} & \cdots & h_{(Q-1)1} \\ h_{12} & \cdots & h_{N2} \\ \vdots & & \vdots \\ h_{(Q-N)J} & \cdots & h_{(Q-1)J} \end{bmatrix} \begin{Bmatrix} B_1 \\ \vdots \\ \vdots \\ B_N \end{Bmatrix} = - \begin{bmatrix} h_{(N+1)1} \\ \vdots \\ h_{Q1} \\ h_{(N+1)2} \\ \vdots \\ h_{QJ} \end{bmatrix}, \tag{A10}$$

or

$$[H]\{B\} = -\{\tilde{h}\}, \tag{A11}$$

which represents $J(Q-N)$ equations in N unknowns (B_q). For $J(Q-N) > N$ an exact solution is not possible, but a least-squares solution can be found by employing the pseudo-inverse of $[H]$:

$$\{B\} = -[H]^{+}\{\tilde{h}\}, \tag{A12}$$

where

$$[H]^{+} = ([H]^{H}[H])^{-1}[H]^{H} \tag{A13}$$

in which ^{H} denotes the complex conjugate transpose. After having found the constants B_q, equation (A7) is solved to give N roots v_n, from which the corresponding complex propagation coefficients ($s_n = -\beta_n - \mathrm{i}k_n$) can be derived,

$$v_n = \mathrm{e}^{s_n \Delta z} = \mathrm{e}^{-\beta_n \Delta z}\, \mathrm{e}^{-\mathrm{i}k_n \Delta z}. \tag{A14}$$

i.e.,

$$k_n = -(1/\Delta z) \arg (v_n), \qquad \beta_n = (1/\Delta z) \log_e (|v_n|). \tag{A15}$$

Finally the amplitudes A_{nj} at the various measurement positions, j, in each wave, n, can be extracted from equation (A3), which can be rewritten in matrix form as

$$\begin{bmatrix} 1 & \cdots & 1 \\ v_1 & \cdots & v_N \\ \vdots & & \vdots \\ v_1^{(Q-1)} & \cdots & v_N^{(Q-1)} \end{bmatrix} \begin{bmatrix} A_{11} & \cdots & A_{1J} \\ \vdots & & \vdots \\ \vdots & & \vdots \\ A_{N1} & \cdots & A_{NJ} \end{bmatrix} = \begin{bmatrix} h_{11} & \cdots & h_{1J} \\ \vdots & & \vdots \\ \vdots & & \vdots \\ h_{Q1} & \cdots & h_{QJ} \end{bmatrix}, \tag{A16}$$

equation (A7) is solved to give N roots v_n, from which the corresponding complex propagation coefficients ($s_n = -\beta_n - \mathrm{i}k_n$) can be derived,

$$v_n = \mathrm{e}^{s_n \Delta z} = \mathrm{e}^{-\beta_n \Delta z}\, \mathrm{e}^{-\mathrm{i}k_n \Delta z}. \tag{A14}$$

i.e.,

$$k_n = -(1/\Delta z) \arg (v_n), \qquad \beta_n = (1/\Delta z) \log_e (|v_n|). \tag{A15}$$

Finally the amplitudes A_{nj} at the various measurement positions, j, in each wave, n, can be extracted from equation (A3), which can be rewritten in matrix form as

$$\begin{bmatrix} 1 & \cdots & 1 \\ v_1 & \cdots & v_N \\ \vdots & & \vdots \\ v_1^{(Q-1)} & \cdots & v_N^{(Q-1)} \end{bmatrix} \begin{bmatrix} A_{11} & \cdots & A_{1J} \\ \vdots & & \vdots \\ \vdots & & \vdots \\ A_{N1} & \cdots & A_{NJ} \end{bmatrix} = \begin{bmatrix} h_{11} & \cdots & h_{1J} \\ \vdots & & \vdots \\ \vdots & & \vdots \\ h_{Q1} & \cdots & h_{QJ} \end{bmatrix}, \tag{A16}$$

or

$$[V][A] = [h]. \tag{A17}$$

For each j, this represents Q equations in N unknowns (A_{nj}). Since $Q > N$, an exact solution is not possible, but once more a least-squares solution can be found, this time by employing the pseudo-inverse of $[V]$:

$$[A] = [V]^{+}[h]. \tag{A18}$$